Investigation of magnetic interaction pathways by experimental electron density measurements: application to an organic free radical, *p*-(methylthio)phenyl nitronyl nitroxide†

Sébastien Pillet,[a] Mohamed Souhassou,[a] Yves Pontillon,[b] Andrea Caneschi,[c] Dante Gatteschi[c] and Claude Lecomte*[a]

[a] *Laboratoire de Cristallographie et Modélisation des Matériaux Minéraux et Biologiques (CNRS UPRESA 7036), Faculté des Sciences, Université Henri Poincaré, Nancy I, BP 239, 54506 Vandoeuvre-lès-Nancy, France. E-mail: lecomte@lcm3b.u-nancy.fr*

[b] *Institut Laue-Langevin, 6 rue Jules Horowitz, BP 156, 38042 Grenoble cedex 9, France*

[c] *Dipartimento di Chimica, Università degli Studi di Firenze, Via Maragliano 77, 50144 Florence, Italy*

Received (in Montpellier, France) 4th May 2000, Accepted 25th July 2000
First published as an Advance Article on the web 20th December 2000

The [X − (X + N)] electron density distribution in a 3D ferromagnetic purely organic free radical, *p*-(methylthio) phenyl nitronyl nitroxide, is reported and analysed in terms of magnetic interactions. From the atomic charges obtained by multipolar refinement against the X-ray data, a charge transfer by intermolecular hydrogen bonds between the O–N–C–N–O fragment of the nitronyl ring and the methylthio group is pointed out. Rotation of the oxygen lone pairs is also observed in the direction corresponding to short intermolecular N–O···O–N contacts. The topological analysis of the electron density allows us to characterise the bonding scheme in this radical and clearly demonstrates an electron delocalisation from the two oxygen to the sulfur atom through the phenyl ring. The atomic vibrations are investigated and their influence on the intermolecular interactions is discussed.

In the last decades, electron density analysis has become a very mature field for the investigation of physical and chemical properties of materials. Among them, charge transfer compounds[1], non-linear optic phenomena,[2–4] hydrogen bond interactions,[5–7] transition metal configurations[8,9] are of important physical and/or chemical interest, but magnetic materials have so far been much less investigated. Until now, only some organometallic compounds, where the magnetic effects on the electron density are more pronounced than in purely organic compounds, have been studied.[10–12]

Nitroxide free radicals,[13] whose magnetic properties are associated with a delocalised unpaired electron ($NO^{\bullet}$, $S = 1/2$), are more and more studied in the field of molecular magnetism.[14–16] They are not only investigated as purely organic radicals but also as efficient ligands in organometallic molecular compounds.[17–20] Among them, nitronyl nitroxide free radicals are probably the most popular. They exhibit a large variety of magnetic behaviour: paramagnetism down to very low temperature,[21] ferromagnetism, antiferromagnetism.[22–29] The crystal packing seems to be a major influence on these features since it rules the occurrence and length of intermolecular contacts that are strongly involved in the magnetic interactions. With the use of the first and second McConnel mechanisms,[30,31] one can sometimes determine whether the intermolecular interactions[32–34] (hydrogen bonds or short N–O···O–N contacts) or a charge transfer[35] involving frontier orbitals are responsible for the magnetic behaviour and dimensionality of such organic radicals. As no systematic trends in the crystal packing[36,37] have yet been found to predict ferro or antiferromagnetic ordering, an effort is still needed to understand the intermolecular interactions.

This paper is devoted to the analysis of the experimental electron density in a nitronyl nitroxide compound, obtained by multipolar refinement against low temperature X-ray measurements. The purpose of this work is to show that meaningful chemical information can be gathered about magnetic interactions in organic free radicals through high resolution X-ray diffraction. This study is based on 2-(4-thiomethyl)phenyl-4,4,5,5-tetramethylimidazoline-1-oxyl-3-oxide [Nit(SMe)Ph, Fig. 1], which orders ferromagnetically at $T_c = 0.2$ K.[39,40] After a brief description of the experimental data collection, we present the methodological background of the structural and multipolar refinements performed. An introduction to the topological analysis of the electron density is also given. In the second part of this paper, we discuss the results obtained from the analysis of the electron density, its deformation density, its topological properties and the molecular and atomic thermal displacements. A direct comparison with the results obtained from polarized neutron diffraction[41,42] is also carried out throughout this paper.

Experimental and methodology

X-Ray diffraction data collection

For X-ray measurements, a parallelepipedic single crystal, prepared as described in the literature,[39] of dimensions $0.30 \times 0.28 \times 0.36$ mm^3 was mounted on a Nonius Kappa-CCD diffractometer using graphite monochromatized Mo-Kα radiation ($\lambda = 0.71073$ Å). The crystal was cooled down to 114 K using a N_2 Oxford cryostream cooling device; the temperature was calibrated using the ADP para-electric antiferroelectric phase transition ($T_c = 148$ K). Initial cell parameters

† Electronic supplementary information (ESI) available: atomic positions and anisotropic displacement parameters refined against the 114 K X-ray and neutron data. See http://www.rsc.org/suppdata/nj/b0/b003674i/

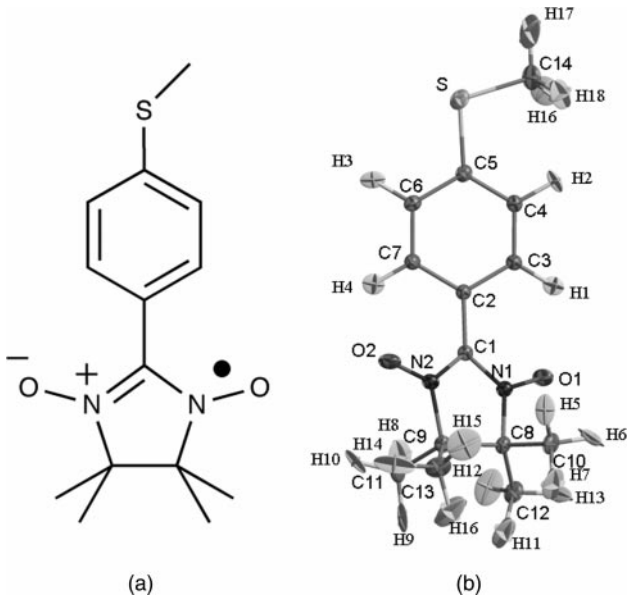

Fig. 1 (a) Chemical structure (H atoms omitted for the sake of clarity) and (b) ORTEP[38] view of Nit(SMe)Ph radical. Thermal ellipsoids are plotted at the 50% probability level.

and orientation matrix were determined by least-squares refinement on 253 reflections measured on 10 frames (oscillation width: 1° per frame, exposure time: 180 s). The final, more accurate cell parameters were obtained at the end of the overall data collection by refinement against all the collected reflections (92 195). Data up to a resolution of 0.91 $Å^{-1}$ were collected in two different detector positions using the ω-scan method. First, 876 images (detector position $\upsilon = 0°$) and second, 1168 images (detector position $\upsilon = 20°$) were measured. For each set, exposure time, oscillation width and detector-to-crystal distance were kept fixed. More details about the experimental settings and crystal data are reported in Table 1. Reflections were integrated using the program DENZO[43] implemented in the HKL package,[43] then sorted and averaged using SORTAV.[44] The crystal did not present any decay during the data collection as checked by the evolution of the inter-frame scale factors *vs.* time. Although tests of empirical absorption corrections (SORTAV[44]) showed that the absorption effect is negligible, the data were corrected. This is in agreement with the low linear absorption coefficient ($\mu_{Mo(K\alpha)} = 0.217$ mm^{-1}) for Nit(SMe)Ph; the resulting maximum and minimum transmission factors are 0.93 and 0.92. The 92 195 observed reflections were merged into 8801 independent reflections with an overall completeness of 98.2% up to the maximum resolution of 0.91 $Å^{-1}$ [99.6% up to (sin $\theta/\lambda = 0.85$ $Å^{-1}$]. The lack of very high resolution X-ray data, which may limit the accuracy of the atomic displacement parameters, will be discussed later. This data collection strategy enabled a high redundancy (10 on average), improving the precision of the intensities that is required for an accurate crystallographic study. Table 2 shows that the internal agreement indice R_{int} is excellent at low resolution and much lower than conventional CAD4 data on the high resolution shells ($R_1 < 5\%$, sin $\theta/\lambda < 0.77$ $Å^{-1}$; great care was taken during data collection to ensure a good signal-to-noise ratio of each intensity peak, even for the high-angle weak reflections, without saturating low-order reflections. The intensity estimated variances were re-estimated using SORTAV,[44] according to the distribution of the multiple intensities around their mean value, as already discussed in a preceding paper.[45]

CCDC reference number 440/230.

Neutron diffraction data collection

A single crystal, in the form of a regular slab of dimension 7.8 × 2.5 × 1.5 mm^3, was used for the neutron experiment. The unpolarised neutron diffraction experiment was per-

Table 1 Experimental and crystallographic details

Chemical formula	$SO_2N_2C_{14}H_{19}$
Formula wt.	279.4
a, *b*, *c*/Å	9.340(2), 19.482(4), 8.634(1)
β/°, *U*/$Å^3$, *Z*	115.13(1), 1422.3(9), 4
Space group, cell setting	$P2_1/a$, monoclinic
T/K, λ/Å	114, Mo(Kα) 0.710 73
μ/mm^{-1}	0.217
X-Ray data collection (Nonius Kappa CCD)	
Scan method, oscillation width/°	ω rotation, 1.5
Exposure time per frame/s	180
Crystal to detector distance/mm	40
No. of frames	2044
Total experimental time/h	~103
No. of measured reflections	92 195
Range of *h*, *k*, *l*	$-15 < h < 15$, $-35 < k < 35$, $-16 < l < 16$
No. of independent reflections	8801
R_{int}[a] (%)	1.8
max(sin θ/λ)/$Å^{-1}$	0.91
Overall completeness (%)	98.2
Neutron data collection (ILL, Grenoble)	
T/K, λ/Å	114, 0.8404
Monochromator	Cu 2 2 0
No. of measured reflections	2217
No. of independent reflections	1880
No. of ind. refl., [$F_o > 4\sigma(F_o)$]	1684
max(sin θ/λ)/$Å^{-1}$	0.58
Range of *h*, *k*, *l*	$-11 < h < 0$, $-11 < k < 23$, $-9 < l < 8$
R_{int}[a] (%)	2.08

$$^{a}R_{int} = \frac{\sum_{H} \sqrt{\frac{N}{N-1}} \sum_{i=1}^{N_{equivalent}} \left| I_i - \langle I \rangle \right|}{\sum_{H} \sum_{i} |I_i|}$$

Table 2 X-Ray data internal agreement indices *vs.* resolution

$S = \sin\theta/\lambda/\text{Å}^{-1}$	N_{terms}	N_{mean}	R_1 [a]	R_2 [b]	R_w [c]
$S < 0.33$	15783	439	1.45	1.68	2.68
$0.33 < S < 0.42$	16446	439	1.70	1.94	3.10
$0.42 < S < 0.48$	14741	448	2.02	2.17	3.92
$0.48 < S < 0.53$	5719	447	2.42	2.65	3.87
$0.53 < S < 0.57$	4275	451	2.43	2.63	3.98
$0.57 < S < 0.61$	4007	454	2.59	2.78	4.28
$0.61 < S < 0.64$	3447	436	2.91	3.05	4.64
$0.64 < S < 0.67$	3286	453	3.15	3.32	4.86
$0.67 < S < 0.70$	3057	432	3.28	3.14	5.31
$0.70 < S < 0.72$	2995	460	3.75	3.78	5.82
$0.72 < S < 0.74$	2616	433	4.11	4.16	6.08
$0.74 < S < 0.77$	2556	442	4.33	4.00	6.69
$0.77 < S < 0.79$	2337	436	5.12	5.00	7.15
$0.79 < S < 0.81$	2104	431	5.48	5.21	7.67
$0.81 < S < 0.83$	2015	436	6.03	5.87	8.42
$0.83 < S < 0.84$	1759	422	6.00	5.70	8.68
$0.84 < S < 0.86$	1512	387	6.89	6.58	9.52
$0.86 < S < 0.88$	1280	374	7.46	6.66	10.84
$0.88 < S < 0.89$	993	329	7.92	8.09	11.25
$0.89 < S < 0.91$	826	281	8.03	7.93	10.47
Total	91759	8430	1.86	1.86	3.92

$$^{a}R_1 = \frac{\sum_H \sqrt{\frac{N}{N-1}} \sum_{i=1}^{N_{\text{equivalent}}} \left| I_i - \langle I \rangle \right|}{\sum_H \sum_i |I_i|} \quad ^{b}R_2 = \sqrt{\frac{\sum_H \sqrt{\frac{N}{N-1}} \sum_{i=1}^{N_{\text{equivalent}}} \left(I_i - \langle I \rangle \right)^2}{\sum_H \sum_i (I_i)^2}} \quad ^{c}R_w = \sqrt{\frac{\sum_H \sqrt{\frac{N}{N-1}} \sum_{i=1}^{N_{\text{equivalent}}} w\left(\frac{I_i - \langle I \rangle}{\sigma(I_i)} \right)^2}{\sum_H \sum_i w\left(\frac{I_i}{\sigma(I_i)} \right)^2}},$$

where w is the weighting scheme.[44]

formed on the D9 diffractometer (four-circle mode) at the ILL reactor (Grenoble, France). The sample was cooled down, using an Air Products Displex cryostat cooling device, to 114 K to match the X-ray experiment temperature. Initial cell parameters and orientation matrix were determined by least-squares refinement on 15 reflections. Final cell parameters were refined with 650 strong reflections after the data collection [$a = 9.3377(4)$, $b = 19.4725(7)$, $c = 8.6305(3)$ Å and $\beta = 115.176(3)°$]. 2217 reflections were collected with $\sin\theta/\lambda$ up to 0.58 Å^{-1} ($\lambda = 0.8404$ Å). Crystal data and experimental parameters, at $T = 114$ K, are reported in Table 1. The calculation of integrated intensities was done by the RACER program[46] during experimental run time. For the averaging of equivalent reflections, the program ARRNGE, based on the Cambridge Crystallographic Library[47] was used. The absorption coefficient $\mu = 0.212$ mm^{-1} was obtained assuming $\sigma = 38$ barn for the hydrogen atoms of the molecule. It was then used to calculate the absorption correction by estimating the mean crystal path for each (*hkl*) reflection collected. The resulting maximum and minimum correction factors $[(I - I_0)/I_0]$ are 23.6 and 16.53%, respectively.

Structural and multipolar refinements

A multipolar model was refined against the X-ray data in order to obtain accurate deformation electron densities. A few parameters (valence and multipolar populations, contraction parameters) were introduced [see eqn. (1) below] in addition to the usual structural refinement. The total electron density can be characterised in a more quantitative way by its topological properties: gradient, density and Laplacian at critical points of the electron distribution.

Crystal structure was refined using MOLLY[48] against neutron diffraction data and lead to the final agreement indices $R = 3.66\%$, $R_w = 2.92\%$, GOF = 2.01 for 1783 reflections and 171 parameters. Hydrogen positions and anisotropic displacement parameters obtained from this measurement are given in the supplementary material.

The X-ray crystal structure was first refined using NRCVAX.[49] Then, the MOLLY multipolar model was applied as defined by:

$$\rho(\vec{r}) = \rho_{\text{core}}(r) + P_{\text{val}}\,\kappa^3\rho_{\text{val}}(\kappa r) + \sum_{l=0}^{l_{\max}} \kappa'^3 R_l(\kappa' r) \sum_{m=0}^{+l} \sum_p P_{lmp}\, y_{lmp}(\theta, \varphi) \qquad (1)$$

where the first two terms $\rho_{\text{core}}(r)$ and $\rho_{\text{val}}(r)$ are the spherically averaged core and valence electron densities of the free atom. The last term is the expansion of the valence density on the y_{lmp} spherical harmonic functions in real form. P_{val} is the valence population, P_{lmp} are the multipole populations and κ, κ' are contraction-expansion parameters. A κ value greater than unity means a contraction of the valence shell of the considered atom whereas a value lower than unity corresponds to an expansion. During refinement, the electro-neutrality of the cell was kept as a constraint. Radial functions $R_l(r)$ were chosen as Slater type [eqn. (2)]

$$R_{n_l}(r) = \frac{\zeta_l^{n_l+3}}{(n_l+2)!}\, r^{n_l} e^{-\zeta_l r} \qquad (2)$$

with the initial n_l and ζ_l parameters being, respectively: 4-4-4-6-8 and 4.87 for the S atom ($l_{\max} = 4$), 2-2-3-4 and 3.00 for O atoms, 2-2-2-3 and 3.00 for N atoms, 2-2-2-3 and 3.14 for phenyl C atoms, 2-2-2-3 and 2.84 for other C atoms ($l_{\max} = 3$), 0-1-1 and 2.00 for H atoms ($l_{\max} = 2$). Radial exponents for the sulfur atom were optimised and a more complete discussion concerning their importance in the refinement can be found elsewhere.[1,50]

Core and valence scattering factors were calculated from Clementi wave functions[51] for the isolated atom and corrections for the anomalous dispersion were made.[52] More information on multipolar models and refinements can be found in references.[53,54]

In the refinement of the electron density, two approaches concerning the hydrogen atom parameters can be followed.

Either H atom positions and thermal parameters are refined against X-ray data only [(X-X) refinement], or these parameters are obtained from neutron diffraction data [X − (X + N)]. With X-ray data only, the refined positions of the hydrogen atoms correspond to the centre of the electron density distribution, which is shifted towards the atom linked to H, therefore shortening the bond. Consequently, this may introduce biases in the electron density modelling and the [X − (X + N)] model was used in this work.

To analyse the electron density fitted by the multipolar model, one can inspect three different density maps. The first type is the experimental deformation density defined by:

$$\Delta\rho_{\text{exp.}}(\vec{r}) = \frac{1}{V}\sum_{\vec{H}}\left(\frac{1}{k}\,|F_{\text{obs}}(\vec{H})|\,e^{i\phi_{\text{multi}}} - |F_{\text{sph}}(\vec{H})|\,e^{i\phi_{\text{sph}}}\right)e^{-2i\pi\vec{H}\cdot\vec{r}} \tag{3}$$

where F_{obs}, F_{sph} are the structure factors observed and calculated at $\vec{H}$ using the spherical atom model, Φ_{mult}, Φ_{sph} are the structure factor phases calculated from the multipolar and spherical model, respectively, k is the scale factor and V is the unit cell volume.

The static deformation density at $\vec{r}$ is defined as the difference between the modelled static total electron density and the spherical averaged independent atoms. This deformation density is expressed as a sum of pseudo-atomic contributions:

$$\Delta\rho_{\text{stat}}(\vec{r}) = \sum_{j=1}^{N_{\text{at}}}\Delta\rho_j(\vec{r} - \vec{r}_j) \tag{4}$$

where the sum is over all the N_{at} atoms of the molecule and the pseudo atomic deformation density deformation is given by:

$$\Delta\rho(\vec{r}) = P_{\text{val}}\,\kappa^3\rho_{\text{val}}(\kappa r) - N_{\text{val}}\,\rho_{\text{val}}(r) + \sum_{l=0}^{l_{\max}}\kappa'^3 R_1(\kappa' r)\sum_{m=0}^{+1}P_{\text{lmp}}\,y_{\text{lmp}}(\theta,\varphi) \tag{5}$$

Finally, the residual density is the difference between modelled and observed electron densities, allowing one to judge the quality of the refinement, and is defined as:

$$\Delta\rho_{\text{resi.}}(\vec{r}) = \frac{1}{V}\sum_{\vec{H}}\left(\frac{1}{k}\,|F_{\text{obs}}(\vec{H})| - |F_{\text{calc}}(\vec{H})|\right)e^{i\Phi_{\text{calc}}}e^{-2i\pi\vec{H}\cdot\vec{r}} \tag{6}$$

F_{obs} and F_{calc} are respectively the structure factors observed and calculated using the multipolar model, Φ_{calc} is the phase calculated from the multipolar model. In this paper, these different densities were calculated and plotted in the phenyl and nitronyl ring planes as well as in three-dimensional representation.

Topology of the electron density

The overall electron density can also be analysed by the "Quantum Theory of Atoms In Molecules" (Bader[55]), which deals with an atomic partition of $\rho(\vec{r})$. From the spatial distribution of the electron density, one can derive the gradient trajectories ($\vec{\nabla}\rho$) and the Laplacian distribution ($\nabla^2\rho$). The gradient paths give evidence of interaction features and allow the location of all critical points (CP) of the electron density where the gradient of ρ vanishes. The sign of the Laplacian is characteristic of an electron accumulation ($\nabla^2\rho < 0$) or depletion ($\nabla^2\rho > 0$). This allows the classification of the bonds as defined by the sign of the Laplacian at the critical point: $\nabla^2\rho < 0$ is observed for open-shell interactions (usually covalent bonds) whereas $\nabla^2\rho > 0$ is observed for closed-shell interactions (usually ionic, hydrogen bonds or van der Waals interactions). The program NEWPROP[56] was used to locate the CP and calculate the topological properties of the modelled electron density in Nit(SMe)Ph. As an example, the gradient paths in the phenyl ring plane are given in Fig. 2(a). The

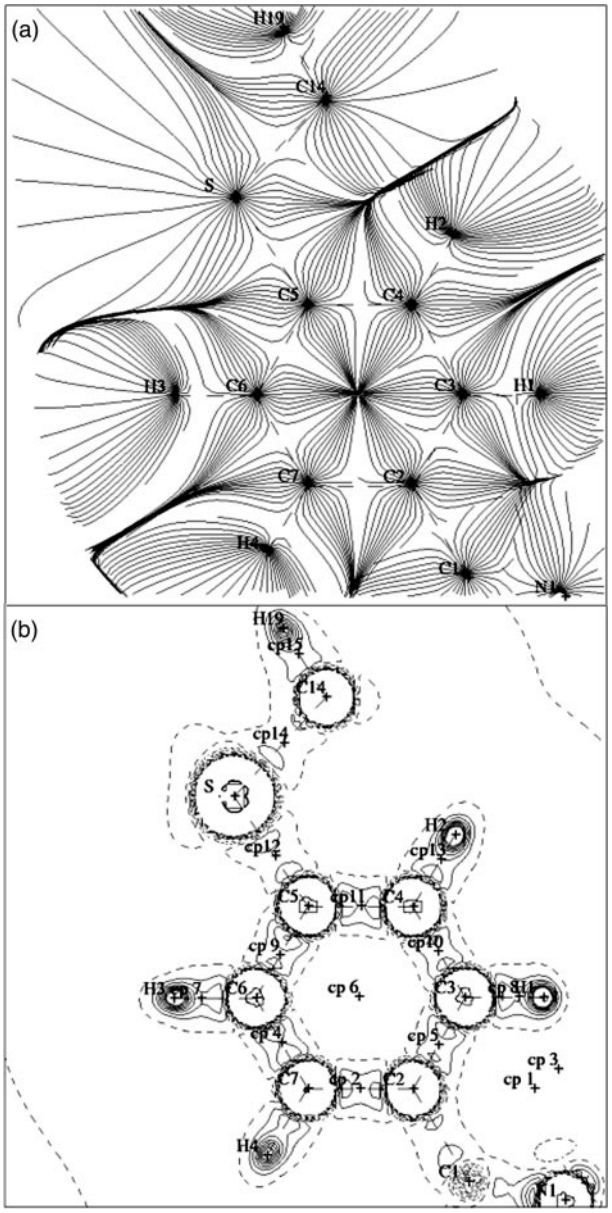

Fig. 2 (a) Gradient trajectories and (b) Laplacian (in e Å^{-5}) of the electron density in the phenyl ring plane ($-\nabla^2\rho$). In (*b*) solid lines represent negative isovalues of the Laplacian of the electron density. Dashed lines are the zero contour and positive isovalues.

trajectories originate at the atomic positions and follow the steepest descent of the electron density. Fig. 2(*b*) presents $-\nabla^2\rho$ in the phenyl ring plane. This shows the shell structure of the atoms (1s for H; 1s, 2s and 2p for C). The Laplacian at the CP is negative, which means an electron concentration in the bonding regions. The ellipticity of a bond as defined by $\varepsilon = 1 - |\lambda_1/\lambda_2|$ (λ_1 and λ_2 being the curvatures of the electron density in the plane perpendicular to the bond, $\lambda_1 < \lambda_2$) represents the deviation from cylindrical symmetry of the electron density ($\varepsilon = 0$ for a pure covalent single bond). The uncertainties of the topological properties are not available, but an estimation of the uncertainties on the position of the critical point is the order of 0.01 Å, the uncertainty on the Laplacian calculated doing only the covariant matrix led to about 10%. So, the errors we estimate are $\sigma(\rho) \approx 0.04$ e Å^{-3} (see later), 0.01 Å for the CP-atom distances and 10% for the curvatures ($\Delta\lambda/\lambda$).

Application of the multipolar refinement to Nit(SMe)Ph

The strategy of the multipole refinement, performed on F, was the following. Position and atomic displacement parameters

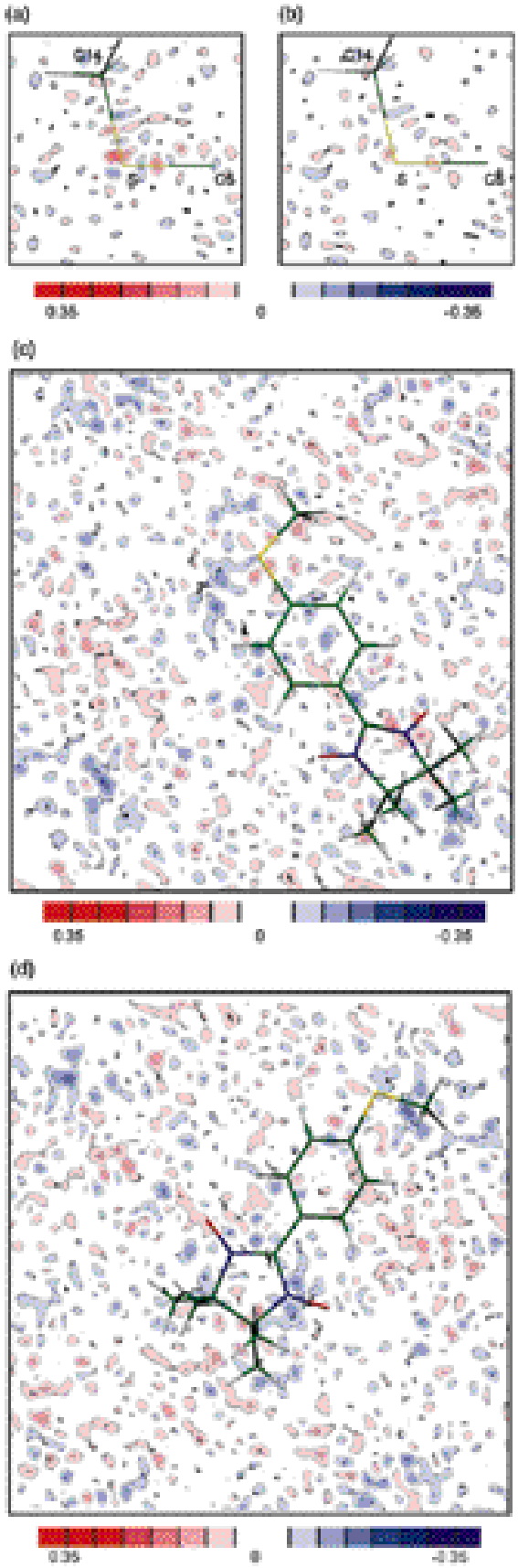

Fig. 3 High order residual density (e Å^{-3}) in the C5–S–C14 plane (a) harmonic model, (*b*) anharmonic [$S_{min} = 0.7$ Å^{-1}, $I > \sigma(I)$] and (c, d) residual density [$I > \sigma(I)$, all data] in the phenyl ring (c) and nitronyl plane (d).

Table 3 Selected bond lengths (Å) and bond angles (°) at the end of the multipolar refinement (model III)[a]

S–C5	1.7571(3)	C3–H1	1.087(4)
S–C14	1.8038(5)	C4–H2	1.103(6)
N1–O1	1.2812(4)	C6–H3	1.096(4)
N2–O2	1.2772(4)	C7–H4	1.071(5)
N1–C8	1.4994(4)	C10–H5	1.095(4)
N2–C9	1.5022(4)	C10–H6	1.094(6)
C8–C9	1.5566(5)	C10–H7	1.088(5)
C8–C12	1.5198(5)	C11–H8	1.104(6)
C8–C10	1.5254(6)	C11–H9	1.094(6)
C9–C13	1.5147(5)	C11–H10	1.082(4)
C9–C11	1.5305(6)	C12–H11	1.088(5)
C2–C1	1.4571(4)	C12–H12	1.077(5)
C2–C3	1.4038(5)	C12–H13	1.090(6)
C3–C4	1.3929(5)	C13–H14	1.082(6)
C4–C5	1.3996(5)	C13–H15	1.088(5)
C5–C6	1.4063(6)	C13–H16	1.086(6)
C6–C7	1.3873(5)	C14–H17	1.094(4)
C7–C2	1.4055(5)	C14–H18	1.093(4)
C1–N1	1.3558(4)	C14–H19	1.091(5)
C1–N2	1.3522(5)		
O1···C4^{i}	3.6656(5)	O2···H17^{ii}	2.678(4)
O1···H1	2.323(4)	O2···C14^{ii}	3.7218(5)
O1···H18^{i}	2.506(4)	O2···H4	2.372(4)
O1···C14^{i}	3.5732(6)	O2···O2^{i}	4.8229(1)
		O2···N2^{i}	4.3827(5)
		O2···H7^{i}	2.336(5)
		O2···C10^{i}	3.3331(5)
X-Ray[b]			
O1···C4^{i}	3.725(5)	O2···C14^{ii}	3.595(5)
O1···C14^{i}	3.896(5)	O2···O2^{i}	4.944(5)
		O2···N2^{i}	4.443(5)
		O2···C10^{i}	3.508(6)
Neutron[c]			
O1···C4^{i}	3.647(6)	O2···C14^{ii}	3.728(4)
O1···C14^{i}	3.540(4)	O2···O2^{i}	4.76(1)
		O2···N2^{i}	4.34(1)
		O2···C10^{i}	3.289(5)
C5–S–C14	103.30(2)	C2–C3–C4	120.79(3)
O2–N2–C9	121.10(3)	C7–C6–C5	120.76(3)
O2–N2–C1	126.63(1)	C3–C4–C5	120.00(4)
O1–N1–C8	121.30(3)	N2–C9–C8	100.88(3)
O1–N1–C1	126.72(3)	N2–C9–C13	109.34(3)
C9–N2–C1	112.17(3)	C8–C9–C13	115.41(3)
C8–N1–C1	111.61(3)	C8–C9–C11	113.34(3)
C3–C2–C7	119.02(3)	C13–C9–C11	110.08(4)
C3–C2–C1	119.79(3)	C2–C7–C6	120.07(2)
C7–C2–C1	121.00(3)	S–C5–C6	116.74(3)
N1–C8–C9	101.25(2)	S–C5–C4	124.05(3)
N1–C8–C12	109.94(2)	N2–C1–N1	108.81(3)
N1–C8–C10	106.00(3)	C6–C5–C4	119.20(3)
C9–C8–C12	114.95(3)	N2–C1–C2	125.01(3)
C9–C8–C10	114.06(2)	N1–C1–C2	125.97(3)
C12–C8–C10	109.88(3)	N2–C9–C11	107.04(3)
O1···H1–C3	115.5(4)	O2···H4–C7	109.3(3)
O1···H18^{i}–C14^{i}	165.1(4)	O2···H17^{i}–C14^{i}	159.3(3)
		O2···H7^{i}–C10^{i}	151.6(4)

[a] Transformations: (*i*) $\frac{1}{2} + x$, $\frac{1}{2} - y$, z; (*ii*) x, y, $1 - z$. [b] From ref. 39: $T = 298$ K, $a = 9.437(2)$, $b = 19.827(2)$, $c = 8.516(2)$ Å, $\beta = 113.33(1)°$. [c] From ref. 42: $T = 10$ K, $a = 9.236(26)$, $b = 19.393(13)$, $c = 8.603(8)$ Å, $\beta = 114.94(1)°$.

(adp) U^{ij} were refined against the high-order reflections (HO): $S = \sin\theta/\lambda \geqslant 0.8$ Å^{-1}, $N_{ref} = 1761$, using a spherical atom model. All hydrogen atoms were found in X-ray Fourier difference maps at a mean 0.98(2) Å C–H distance. This gave model I (IAM, X-X). Positions and adps for H atoms obtained from neutron diffraction lead to model I′ [IAM, X-(X + N)], the mean C–H distance being 1.090(6) Å. As shown on the residual density plot [Fig. 3(a)], the S atom thermal displacement was insufficiently described by a harmonic model. Hence, the HO residual density presents a three-fold symmetry of alternating positive and negative densities. Therefore, an anharmonicity model using the Gram–Charlier

expansion[57] was applied [eqn. (7)]:

$$T_{\text{anharmo}}(\vec{H}) = T_{\text{harmo}}(\vec{H}) \times \left[1 + \frac{(2\pi i)^3}{3!} C^{ijk} h_i h_j h_k + \frac{(2\pi i)^4}{4!} D^{ijkl} h_i h_j h_k h_l\right] \quad (7)$$

$$T_{\text{harmo}}(\vec{H}) = e^{-2\pi^2 h_i h_j a^i a^j U^{ij}} \quad (8)$$

where U^{ij}, C^{ijk} and D^{ijkl} are the least-squares refined coefficients (18 of these 25 coefficients had values greater than one esd). This anharmonic model led to a cleaner residual density [Fig. 3(b)] around the sulfur atom and consequently slightly improved the agreement factors (R decreased from 3.44% to 3.40% and R_w from 5.84 to 5.82%). Therefore, this anharmonic model was used in all subsequent refinements. From the S atom mean position (x_0) and thermal parameters, one can define a probability density function (pdf) describing in real space the atomic motion from the mean position in a harmonic or anharmonic potential. The pdf is the inverse Fourier transform of the atomic temperature factor $T(\vec{H})$ and has an anisotropic Gaussian form in the usual case of a harmonic potential. The anharmonic pdf was calculated and analysed for sulfur atom and compared to the harmonic one as discussed later.

Once the x, y, z, U^{ij} parameters are known, the valence populations (P_{val}) and contraction-expansion (κ) parameters were refined using the P_{val}-κ model.[58] The κ parameters for chemically equivalent C atoms were constrained: one κ for the sp^2 C atoms and one for the sp^3. This led to model II. Finally, a full multipolar model (model III) without any intensity sigma cutoff was performed ($N_{\text{ref}} = 8801$). In all refinements, the P_{lmp} parameters of both nitrogens were imposed to be equal. Since a preliminary refinement only allowed us to distinguish between methyl or phenyl hydrogen atoms (all P_{lmp} parameters were equal within σ), two types of hydrogen atoms were defined: phenyl (sp^2) or methyl (sp^3) ones. This allowed the number of parameters to be decreased. Atomic positions and adps at the end of refinement III are given in the electronic supplementary material whereas selected 114 K interatomic distances and angles are given in Table 3.

Results

Multipolar refinement results

Table 4 summarises the agreement indices corresponding to the independent atom model (I and I′, H_X = atomic parameters obtained from X-ray data, H_N = atomic parameters from neutron data), P_{val}-κ model (II) and multipolar model (III). These agreement factors decreased from ($R = 4.27$, $R_w = 5.14\%$ and GOF = 1.56) for model I to ($R = 2.95$, $R_w = 2.85\%$ and GOF = 0.86) for the full multipolar model III. One remark can be made on these final values of the agreement factors: the R_w value is very close to the R value, which means that the esds on the intensities calculated from SORTAV[44] are well estimated, and even slightly overestimated as suggested by the lower than unity value of the GOF. The residual density at the end of the multipolar refinement is clear both in the phenyl ring plane [Fig. 3(c)] and in the nitronyl ring plane [Fig. 3(d)], which shows the quality of the data and the accuracy of the fitted electron density. The estimated standard deviation (esd) on the electron density as defined in eqn. (9) is 0.04 e Å^{-3}, in agreement with the average esd of F.

$$\sigma(\rho) = \frac{\sum_{\vec{H}} |\Delta F(\vec{H})|}{V} \quad (9)$$

where $\Delta F(\vec{H})$ is the difference between observed and calculated structure factor.

As written above, an anharmonic model was used to accurately describe sulfur atomic motions. The probability density function in the anharmonic model [Fig. 4(b)], calculated using PROMETHEUS,[59] is very close to that derived from the harmonic model [Fig. 4(a)], indicating that anharmonicity on the sulfur atom is only a small correction to its thermal motion.

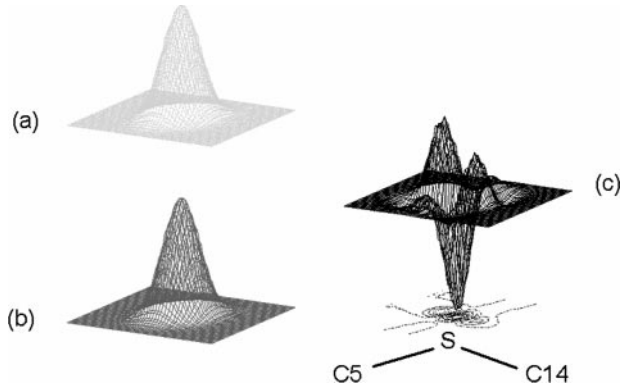

Fig. 4 Probability density functions of the sulfur atom in the C5–S–C14 plane: (a) harmonic and (b) anharmonic model. (c) Difference between the function in (b) and (a) on a ×40 scale.

Table 4 Agreement indices for the different refined models

	Model I Spherical atom model (H_X)	Model I′ Spherical atom model (H_N)	Model II[a] P_{val}-κ model (H_N)	Model III Multipolar model
N_{obs} ($0\sigma/3\sigma$)	8801/6861	8801/6861	8801/6861	8801/6861
N_{par}	273	197	225	560
R ($0\sigma/3\sigma$)[b]	4.27/3.14	4.51/3.40	4.38/3.26	2.95/1.81
R_w ($0\sigma/3\sigma$)[c]	5.14/4.85	6.06/5.82	5.32/5.05	2.85/2.36
GOF ($0\sigma/3\sigma$)[d]	1.56/1.67	1.82/1.98	1.61/1.73	0.86/0.80

[a] Model II was refined with the x, y, z, U^{ij} parameters of model III. [b] $R = \dfrac{\sum_{\vec{H}} \left| \frac{1}{k} |F_{\text{obs}}(\vec{H})| - |F_{\text{calc}}(\vec{H})| \right|}{\sum_{\vec{H}} \frac{1}{k} |F_{\text{obs}}(\vec{H})|}$,

[c] $R_w = \sqrt{\dfrac{\sum_{\vec{H}} w \left[\left| \frac{1}{k} |F_{\text{obs}}(\vec{H})| - |F_{\text{calc}}(\vec{H})| \right| \right]^2}{\sum_{\vec{H}} \frac{1}{k^2} w |F_{\text{obs}}(\vec{H})|^2}}$, [d] $\text{GOF} = \sqrt{\dfrac{\sum_{\vec{H}} w \left[\left| \frac{1}{k} |F_{\text{obs}}(\vec{H})| - |F_{\text{calc}}(\vec{H})| \right| \right]^2}{N_{\text{obs}} - N_{\text{var}}}}$, $w = \sigma^{-2}(F)$

Fig. 4(c) shows the difference between the anharmonic and the harmonic pdfs as a relief map in the C5–S–C14 plane. The main feature is a double positive peak surrounding a negative hole in the S–C14 direction, at about 0.25 Å from the sulfur atom. This means that the sulfur atom motion is slightly more elongated in this direction than as described by the harmonic model.

The thermal displacement tensors of the Nit(SMe)Ph radical were also analysed using the TLS[60] formalism (see below). In a first step, the molecule was considered as a rigid unit called the rigid-body model[61] whose displacement is described by matrix $\boldsymbol{U}_{\mathrm{mol}}$ [eqn. (10)]:

$$U_{\mathrm{mol}} = \begin{pmatrix} \boldsymbol{T} & \boldsymbol{S} \\ (\boldsymbol{S}^*)^{\mathrm{T}} & \boldsymbol{L} \end{pmatrix} \qquad (10)$$

where the $\boldsymbol{T}$, $\boldsymbol{L}$ and $\boldsymbol{S}$ matrices represent: the translation matrix, $\boldsymbol{T} = \langle uu^{\mathrm{T}} \rangle$, the libration matrix: $\boldsymbol{L} = \langle \upsilon\upsilon^{\mathrm{T}} \rangle$ and the correlation (cross) matrix: $\boldsymbol{S} = \langle u\upsilon^{\mathrm{T}} \rangle$. u is the translational displacement of the molecule from its equilibrium position and υ its angular displacement. The coefficients of the $\boldsymbol{T}$, $\boldsymbol{L}$ and $\boldsymbol{S}$ matrices were refined using the program EKRT[62] by least-squares fit against the observed atomic displacement parameters (adp) previously obtained from refinement of model III. At this stage, the agreement indices of the fit were: $R_{\mathrm{w}} = 9.4\%$, GOF = 19.7 (R_{w} and GOF defined in Table 5 caption). As these figures of merit are high, this free radical Nit(SMe)Ph cannot be considered as a rigid unit; whereas the Us of all phenyl C atoms are low and almost isotropic (Fig. 1), the thermal vibration is much higher and more anisotropic for all other atoms. Chemical sensitive internal motions were added in the thermal model and TLS refinement: among them, three motions describing the vibration of the four methyl groups linked to the nitronyl ring (C10, C11, C12, C13), three others describing the vibration of the methylthio fragment and two internal vibrations for the oxygen atoms (Fig. 5). The agreement indices decreased to $R_{\mathrm{w}} = 5.3\%$ and GOF = 11.6. Table 5 summarises the T, L and S parameters and the amplitudes of the refined internal vibrations with respect to the inertial axis of the molecule. The main characteristics, which can be related to the magnetic interactions, are an external libration [3.3(2)°] of the molecule along the Z principal axis (nearly parallel to the C1–C2 direction), a libration of the C5–S–C14 angle [5.5(8)°], and a bending of the C1–N2–O2 [3.0(2)°] and C1–N1–O1 [3.5(1)°] angles. Furthermore, as shown by the Hirshfeld rigid-bond test[63] (Table 6), large differences (ΔZ) occur for all bonds involving a methyl group; S–C14, C8–C12, C9–C13 and C9–C11, which may suggest a possible static disorder that was impossible to resolve at this experimental resolution.[64]

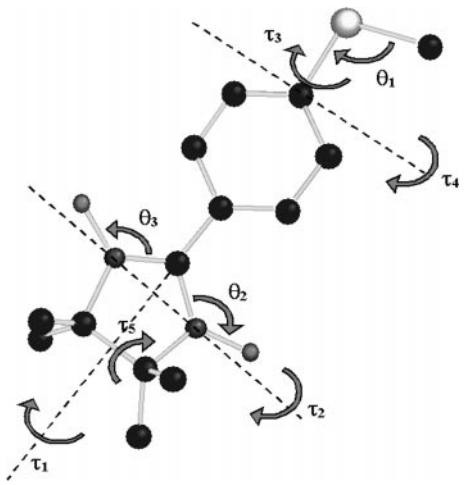

Fig. 5 View and labelling of the internal vibrations. θ_i are in-plane bendings and τ_i are torsional librations.

Table 5 Parameters of the TLS model and internal motion angles

Translational tensor	
Principal values/Å^2	0.0150(6)
	0.0144(4)
	0.0146(2)
Librational tensor	
Principal values/°^{2}	1.8(1)
	1.2(1)
	11(1)
Squared internal vibrations[a]/°^{2}	
τ_1	20(5)
τ_2	10(2)
τ_3	−30(5)
τ_4	−10(4)
τ_5	7(3)
θ_1	13(2)
θ_2	9(3)
θ_3	12(3)
TLS model	
R_{w},[b] GOF[c]	0.094, 19.7
Full model (TLS + int. vib.)	
R_{w},[b] GOF[c]	0.053, 11.6

[a] τ_i is a torsional libration about a bond, θ_i is an in-plane bending around an atom. Principal values are given with respect to the inertial principal axis of the molecule. Z principal axis is nearly directed along the C1–C2 bond. [b] $R_w = \sqrt{\dfrac{\sum\left(\dfrac{\Delta U^{ij}}{\sigma(U^{ij})}\right)^2}{\sum\left(\dfrac{U^{ij}}{\sigma(U^{ij})}\right)^2}}$ [d] [c] $\mathrm{GOF} = \sqrt{\dfrac{\sum\left(\dfrac{\Delta U^{ij}}{\sigma(U^{ij})}\right)^2}{N_{\mathrm{obs}} - N_{\mathrm{par}}}}$ [d] ΔU^{ij} is the difference between "observed" (see text) and calculated adp, N_{obs} is the number of observations (6 U^{ij} per non-hydrogen atom, *i.e.* $N_{\mathrm{obs}} = 114$) and N_{par} is the number of refined parameters ($N_{\mathrm{par}} = 28$).

Structure analysis

The Nit(SMe)Ph structure has been previously discussed from room temperature X-ray measurements[39] and from 10 K neutron measurements.[42] The chemical structure and the

Table 6 Results of the Hirshfeld rigid-bond test

X–Y bond	Z(X)[a]/Å^2	Z(Y)[a]/Å^2	ΔZ[b]/Å^2
S–C5	0.027 133	0.022 469	−0.004 664
S–C14	0.043 186	0.054 820	0.011 634
C2–C1	0.019 710	0.019 741	0.000 031
Phenyl ring			
C2–C3	0.025 299	0.029 255	0.003 956
C3–C4	0.025 831	0.028 706	0.002 874
C4–C5	0.011 310	0.013 742	0.002 432
C5–C6	0.031 976	0.030 373	−0.001 603
C6–C7	0.023 733	0.024 688	0.000 955
C7–C2	0.010 073	0.010 148	0.000 076
Nitronyl ring			
N1–O1	0.019 881	0.023 051	0.003 170
N2–O2	0.015 322	0.014 239	−0.001 083
N1–C8	0.018 261	0.017 716	−0.000 545
N2–C9	0.021 174	0.019 823	−0.001 351
C8–C9	0.021 997	0.021 441	−0.000 557
C8–C12	0.020 768	0.029 925	0.009 157
C8–C10	0.015 159	0.015 542	0.000 383
C9–C13	0.013 496	0.015 565	0.002 069
C9–C11	0.024 836	0.035 210	0.010 373

[a] Z(X) and Z(Y) are the components of the thermal ellipsoids of atoms X and Y along the bond direction. [b] ΔZ is the difference between Z(X) and Z(Y).

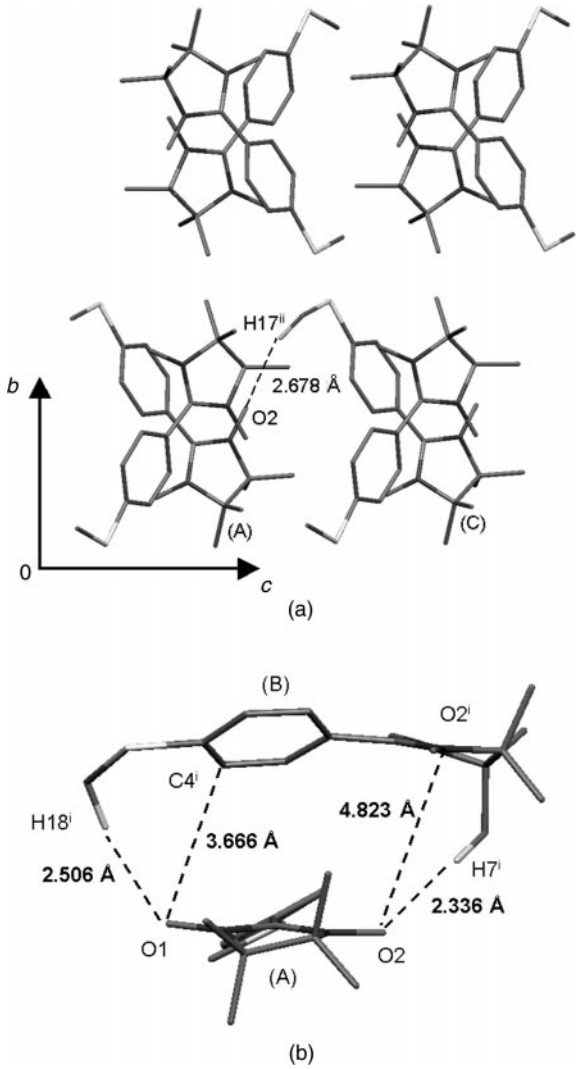

Fig. 6 View of the crystal packing and intermolecular contacts of Nit(SMe)Ph. Only the H atoms involved in the contacts are represented (*i.e.*, $H7^{i}$, $H17^{ii}$ and $H18^{i}$). Molecule B (*a*) is related to molecule A by the glide plane $(1/2 + x, 1/2 - y, z)$ and molecule C (*b*) by the cell translation $(x, y, 1 - z)$.

labelling scheme are summarised in Fig. 1, the crystal packing[65] and the shortest intermolecular contacts are given in Fig. 6. In the *a* direction, the nitronyl rings are stacked nearly parallel to each other and the phenyl ring is twisted around the C1–C2 bond by 32.51(1)°. The crystal packing implies different intermolecular contacts, which involve both nitroxide fragments N1–O1 and N2–O2, in the *a* and *c* directions. The two oxygen atoms first exhibit intramolecular contacts with the closest hydrogen atom of the phenyl ring with $d_{O1\cdots H1} = 2.323(4)$ and $d_{O2\cdots H4} = 2.372(4)$ Å, respectively. They are also both linked by intermolecular hydrogen bonds to the methylthio group: O2 along the *c* axis with $H17^{ii}$ [$d_{O2\cdots H17} = 2.678(4)$ Å] and O1 along the *a* axis with $H18^{i}$ [$d_{O1\cdots H18} = 2.506(4)$ Å]. In the *a* direction, O1 is close to $C4^{i}$ with a distance of $d_{O1\cdots C4} = 3.6656(5)$ Å. Along this axis, the N2–O2 groups of adjacent molecules are nearly perpendicular with a distance of 4.3827(5) Å between O2 and $N2^{i}$. Finally, O2 is also involved in an intermolecular contact with $H7^{i}$ [$d_{O2\cdots H7} = 2.336(5)$ Å] of a methyl group bonded to the nitronyl ring. Furthermore, the bond lengths N1–O1 and N2–O2 are slightly different [1.2812(4) and 1.2772(4) Å, respectively], N2–O2 being shortened by 0.005 Å compared to the value at room temperature[39] [1.283(5) Å]. This distinction in bond length between N1–O1 and N2–O2 is also observed at 10 K. The length of these intermolecular contacts changes significantly with temperature, from 298 to 114 and to 10 K (Table 3), and may be correlated to the evolution of the cell parameters: *c* increases by 1.0% whereas *a* and *b* decrease by 2.2% and 2.1%, respectively. Therefore, the $O2\cdots C14^{ii}$ contact is lengthened by 0.133 Å. The distance between the nitroxide fragments decreases by 0.103 and 0.184 Å for $O2\cdots N2^{i}$ and $O2\cdots O2^{i}$ and the $O1\cdots C4^{i}$ distance follows the same trend. The most spectacular change is for $O1\cdots C14^{i}$ whose distance decreases by nearly 0.356 Å. In summary, the two nitroxide fragments are involved in a network of hydrogen bonds and N–O···O–N contacts in the *a* and *c* directions whose study is of major importance to understand the low temperature magnetic behaviour of Nit(SMe)Ph.

As discussed before, the rigid-body model was insufficient to satisfactorily describe the observed thermal motion of the Nit(SMe)Ph radical (Fig. 1), and internal vibrations had to be added to the model. Among them, some may influence the magnetic interactions. The angles θ_3 and θ_1 (Fig. 5), which are respectively a rotation of the C14 methyl group around the C5–S bond and a bending of the S–C14 bond, can influence the strength of the intermolecular interactions $C14^{ii}$–$H17^{ii}\cdots O2$ and $C14^{i}$–$H18^{i}\cdots O1$ by their vibrational amplitudes. Therefore, at very low temperature, such interactions should be stronger, thus facilitating the magnetic interactions through these pathways. The θ_2 and θ_3 angles represent a bending of the two N–O bonds in the phenyl ring plane. As shown on Fig. 1, the two oxygen atoms are vibrating strongly in the *a* direction, which is the direction of the intermolecular contacts between two symmetry related N–O groups [4.3827(5) Å between O2 and $N2^{i}$; Fig. 6]. This phenomenon persists to very low temperatures and was also observed at 10 K.[42] Furthermore, the external libration of the whole molecule is more important around the inertial *Z* axis (3°). This is consistent with the fact that the oxygen atoms, which are the most distant from this axis, are vibrating strongly in the *a* direction. This libration changes the distance between the two N2–O2 groups of the two adjacent molecules related by the symmetry operation $1/2 + x$, $1/2 - y$, z. This is striking considering the several intramolecular and intermolecular interactions in which the oxygen atoms are involved, which should immobilise them.

Deformation density and topological properties

The experimental deformation density, which includes thermal smearing effects and experimental noise is given in Fig. 7. The bonding densities in the phenyl bonds ($\rho_{max} = 0.45$ e Å^{-3}) are equal to each other within sigma (0.04 e Å^{-3}) and the two N–O bonds are rather similar (0.2 e Å^{-3}). The maximum of deformation density in the bridging C1–C2 bond (0.4 e Å^{-3}) is slightly lower than in the phenyl ones and the two S–C bonds differ, 0.3 and 0.2 e Å^{-3} for S–C5 [$d = 1.7571(3)$ Å] and S–C14 [$d = 1.8038(5)$ Å] respectively. Fig. 8(a,b) present the static deformation density sliced in the plane of the phenyl ring and the nitronyl ring, respectively. They show the same characteristics as the experimental density but without thermal smearing effects and noise, therefore increasing the bonding electron density. All C–C phenyl peaks are equal ($\langle\rho_{C-C}\rangle = 0.65$ e Å^{-3}), which is in close agreement with the results obtained in the tryptophane ring of *N*-acetyl-L-tryptophan-*N*-methylamide: Ac–tr[66] (0.60 to 0.65 e Å^{-3}) where the phenyl ring is also highly involved in a conjugated system (indole ring). The bridging C1–C2 bond shows a higher deformation density than for a single C–C with a maximum of 0.50 e Å^{-3}, compared to the C8–C9 single bond whose maximum is only 0.40 e Å^{-3}. The average deformation density in the two N–O bonds is 0.35 e Å^{-3}. The two short C–N bond [$d_{C1-N2} = 1.3522(5)$ and $d_{C1-N1} = 1.3558(4)$ Å] densities are equivalent (0.60 e Å^{-3}) whereas the corresponding densities are only 0.30 e Å^{-3} for the two long C–N bonds [$d_{C8-N1} = 1.4994(4)$ and $d_{C9-N2} = 1.5022(4)$ Å]. The two S–C

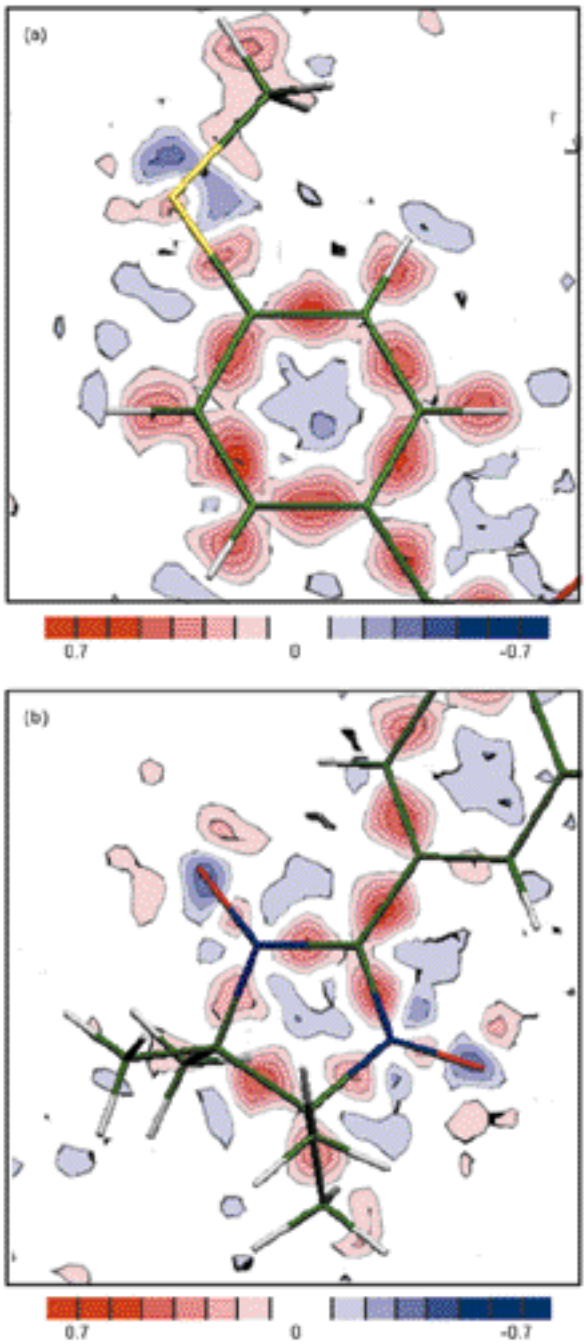

Fig. 7 Experimental deformation density (in e Å^{-3}) in (a) the phenyl ring and (b) nitronyl ring plane [$I > \sigma(I)$, all resolution range].

bonds present nearly the same deformation density (0.30 e Å^{-3}) even if the bond lengths are significantly different [1.7571(3) Å for S–C5, 1.8038(5) Å for S–C14]. The sulfur lone pairs lie in the plane bisecting the C5–S–C14 angle and are tetrahedrally oriented with respect to the two S–C bonds [Fig. 8(c)]. The lone pair density above the phenyl plane is higher (0.5 e Å^{-3}) than the one below (0.2 e Å^{-3}).

The atomic valence populations, P_{val}, calculated from the P_{val}-κ refinement using positions and atomic displacement parameters obtained from model III, give chemically meaningful information about the interactions in Nit(SMe)Ph (Table 7). Whereas the methylthio group is highly negative [−0.60(3) e], each N–O fragment is less negative [−0.16(1) e] than expected for such electronegative atoms.[67,68] The bridging C1 and C14 atoms are more negative [P_{val} = 4.29(2) and 4.27(2) e, respectively] than all the other carbon atoms; the mean valence population is 4.03(2) e for the phenyl carbons and 3.91(2) e for the methyl (C10, C11, C12 and C13) carbons. Methyl fragments of the nitronyl ring are positive, the net fragment charge ranging from +0.27(4) e to +0.40(4) e. The contraction-expansion κ parameters obtained at the end of refinement are lower than unity for all atoms, which means a global expansion of the valence electron density of the radical towards its neighbours.

Once the deformation density is described, a more quantitative discussion may be performed through the topological analysis. Table 8 sums up the critical point (CP) and topological properties for all bonds in Nit(SMe)Ph. The values obtained for C–C phenyl bonds (ρ = 2.06 e Å^{-3}, $\nabla^2\rho$ = −18.0 e Å^{-5}, ε = 0.22) are in close agreement with those reported for the six-membered ring of the indole group in the peptide Ac–tr[66] (ρ = 2.05 e Å^{-3}, $\nabla^2\rho$ = −16.0 e Å^{-5}, ε = 0.19). Furthermore, the electron density and the Laplacian are lower than those obtained for the phenyl ring in *N*-acetyl-α,β-dehydrophenylalanine-*N*-methylamide[69] (ρ = 2.21 e Å^{-3}, $\nabla^2\rho$ = −20.3 e Å^{-5}, ε = 0.23); this results from the delocalization effects in Nit(SMe)Ph, which decrease the electron density in the phenyl bond and increase it in the other bonds involved in the delocalization (S–C5, C1–C2). The electron density in the S–C bonds at the CP is smaller than that observed in C–C bonds. The topological properties of the short S–C5 bond CP differ from those of the long S–C14 bond: the electron density, the negative Laplacian and the ellipticity are higher (1.31 e Å^{-3}, −7.11 e Å^{-5} and 0.18 compared to 1.23 e Å^{-3}, −5.42 e Å^{-5} and 0.11, respectively). These differences are due to the partial π character of the short bond. Whereas S–C5 features are consistent with the S–C bonds observed in the BTDMTTF-TCNQ complex[1] (d = 1.739 Å, ρ = 1.32 e Å^{-3}, $\nabla^2\rho$ = −2.75 e Å^{-5}), the topological features in S–C14 present the same properties as the corresponding S–C single bonds in L-cystine.[50] The C1–C2 bond topological properties are closer to those of the phenyl C–C bonds than to those of a pure single C–C bond (C8–C9): short distance [1.4571(4) Å], high electron density (1.80 e Å^{-3}) and high negative Laplacian (−13.21 e Å^{-5}) at CP. The same conclusions can be drawn for the two short C–N bonds (C1–N1 and C1–N2) compared to the two single C–N bonds

Table 7 Atomic valence populations and κ parameters at the end of multipolar refinement (model III)

Atom	P_{val}	κ	Atom	P_{val}	κ
S	6.54(3)	0.956(1)	C7	4.10(2)	0.986(1)
O1	6.07(1)	0.968(1)	C8	4.09(2)	0.967(1)
O2	6.05(1)	0.968(1)	C9	4.05(2)	0.967(1)
N1	5.09(1)	0.983(1)	C10	3.97(2)	0.967(1)
N2	5.11(1)	0.983(1)	C11	3.92(2)	0.967(1)
C1	4.29(2)	0.967(1)	C12	3.82(2)	0.967(1)
C2	3.91(2)	0.986(1)	C13	3.95(2)	0.967(1)
C3	4.24(2)	0.986(1)	C14	4.27(2)	0.967(1)
C4	4.01(2)	0.986(1)	H(methyl)	0.927(3)	0.979(2)
C5	3.95(2)	0.986(1)	H(phenyl)	0.934(3)	0.979(2)
C6	3.95(2)	0.986(1)			

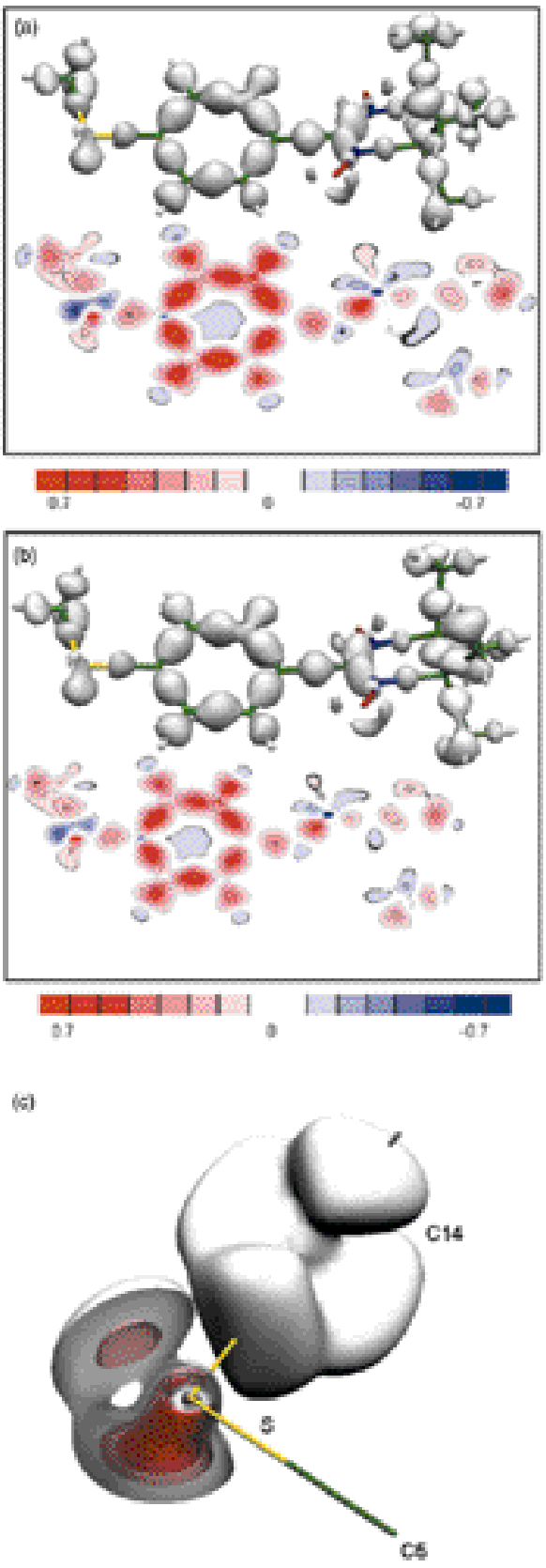

Fig. 8 Three-dimensional representation of the static deformation density (in e $Å^{-3}$) in (a) the phenyl ring plane, (b) nitronyl ring plane and (c) C5–S–C14 plane. The sections of the static deformation density in the phenyl and nitronyl rings are projected at the bottom of each frame. In (a) and (b), the isocontour is plotted at the 0.2 e $Å^{-3}$ level. In (c), isocontours are plotted at the 0.1 e $Å^{-3}$ level. The section of the static deformation density is in the plane bisecting the C5–S–C14 angle.

(C9–N2 and C8–N1). Therefore, the four bonds S–C5, C1–C2, C1–N1 and C1–N2 share a common characteristic: a mixed π-σ character that is due to the delocalisation from the two O to S atoms, thus increasing the S negative net charge. The two N–O bond features are slightly different [$\rho = 2.63$ and 2.74 e $Å^{-3}$, $\nabla^2\rho = 7.84$ and 2.00 e $Å^{-5}$, $\varepsilon = 0.14$ and 0.11 for N1–O1 and N2–O2, respectively), but we have to note that the N–O electron density is not as accurate as for the other atoms of the molecule, due to the high thermal displacement parameters of the oxygen atoms. The Laplacian at the N–O CP is surprisingly positive, which is characteristic of closed shell interactions, although high electron density is observed in the bond (2.69 e $Å^{-3}$ on average for the two N–O bonds).

The two oxygen atoms differ by the intra- and intermolecular contacts in which they are involved (Fig. 6). The two oxygen atoms are linked by intramolecular hydrogen bonds to the closest phenyl hydrogen atom, forming two six-membered rings (C1–C2–C3–H1···O1–N1 and C1–C2–C7–H4···O2–N2). In each bond, the electron density and Laplacian at the CP are high (0.09 and 0.09 e $Å^{-3}$, 1.52 and 1.41 e $Å^{-5}$, respectively), indicating strong hydrogen bonds.[7] The O2 lone pairs are deformed and partially rotated in the direction of the

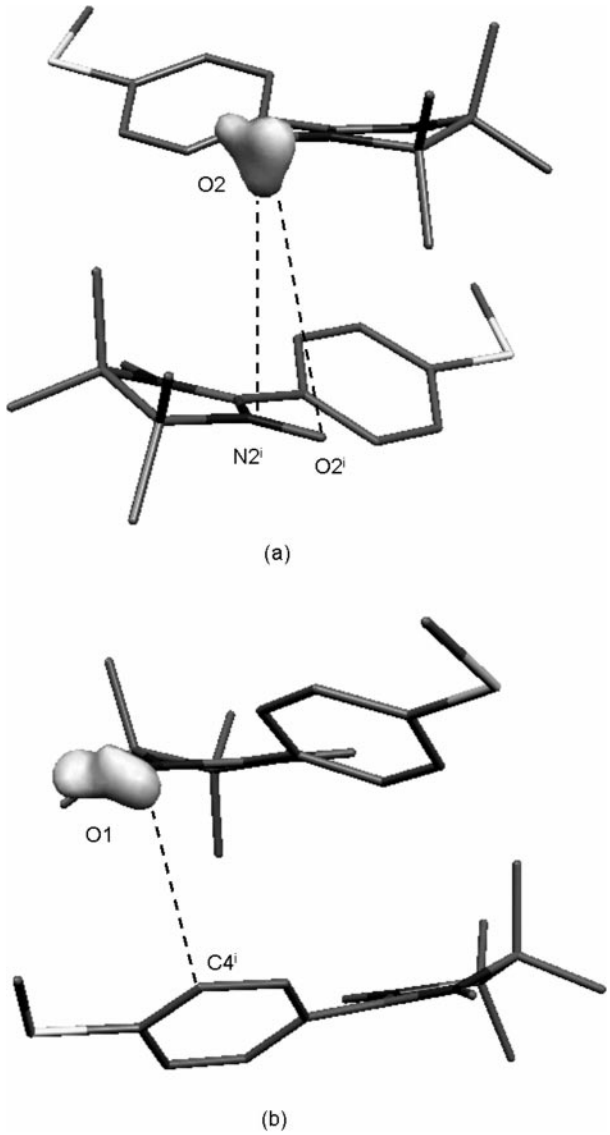

Fig. 9 Static deformation density (in e $Å^{-3}$) in the intermolecular contacts (a) O2···N2^i and (b) O1···C4^i. H atoms are omitted and only the O1 and O2 deformation density is represented for the sake of clarity. Isocontour is plotted at the 0.1 e $Å^{-3}$ contour. The intermolecular contacts O2···O2^i, O2···N2^i and O1···C4^i are given by dashed lines.

Table 8 Topological properties of the bond critical points

X–Y bond[a]	d(X–Y)/ Å	d(X–CP)/ Å	d(Y–CP)/ Å	$\rho(r_{CP})$/ e Å^{-3}	$\rho - \rho_{pro}$[b]/ e Å^{-3}	$\nabla^2\rho(r_{CP})$/ e Å^{-5}	ε
S–C5	1.657	0.946	0.811	1.31	0.33	−7.11	0.18
S–C14	1.802	0.948	0.854	1.23	0.30	−5.42	0.11
$(C–C)_{phenyl}$	1.400	0.700	0.700	2.06	0.65	−18.00	0.22
C1–C2	1.457	0.796	0.661	1.80	0.52	−13.21	0.07
C1–N1	1.357	0.533	0.824	2.22	0.55	−18.31	0.24
C1–N2	1.352	0.523	0.829	2.20	0.52	−18.13	0.22
N1–O1	1.281	0.640	0.641	2.63	0.16	7.84	0.14
N2–O2	1.277	0.638	0.639	2.74	0.25	2.00	0.11
N1–C8	1.501	0.861	0.640	1.57	0.28	−7.22	0.11
N2–C9	1.503	0.861	0.642	1.59	0.30	−7.36	0.11
C8–C9	1.556	0.785	0.771	1.58	0.49	−11.09	0.13
O2···H4	2.492	1.405	1.087	0.09	[c]	1.41	
O2···H17^{ii}	2.686	1.552	1.134	0.03	0.00	0.50	
O1···H1	2.404	1.387	1.017	0.09	[c]	1.52	
O2···H7^{i}	2.356	1.364	0.992	0.06	−0.03	1.12	
O1···H18^{i}	2.514	1.450	1.064	0.05	0.00	0.73	

[a] (*i*) 1/2 + *x*, 1/2 − *y*, *z*; (*ii*) *x*, *y*, 1 − *z*. [b] ρ_{pro} is the promolecule electron density (*i.e.*, the sum of independent spherical atoms). [c] The critical point is not defined in the promolecule.

neighbouring N2^{i}–O2^{i} group [Fig. 9(a)]. Fig. 9(b) shows weaker effects, hardly significant, between O1 and C4. The molecule and its equivalent by a *c* lattice translation are not fully isolated as shown on Fig. 10(a). A 0.03 e Å^{-3} isocontour links the two molecules in the O2···H17^{ii}–C14^{ii} direction, the line on which a bond CP was found. This shows the presence of an electron density continuum in the direction between the two molecules. This is also the case for the O1···H18^{i}–C14^{i} and O2···H7^{i}–C10^{i} contacts [Fig. 10(b)]. In both contacts, a significant electron density (0.05 e Å^{-3}) located right on the O···H axis, is characteristic of a hydrogen bond. The electron density at CP is lower in the O2···H17^{ii} intermolecular contact (0.03 e Å^{-3}) than in the two other ones (ρ = 0.05 and 0.06 e Å^{-3}, respectively).

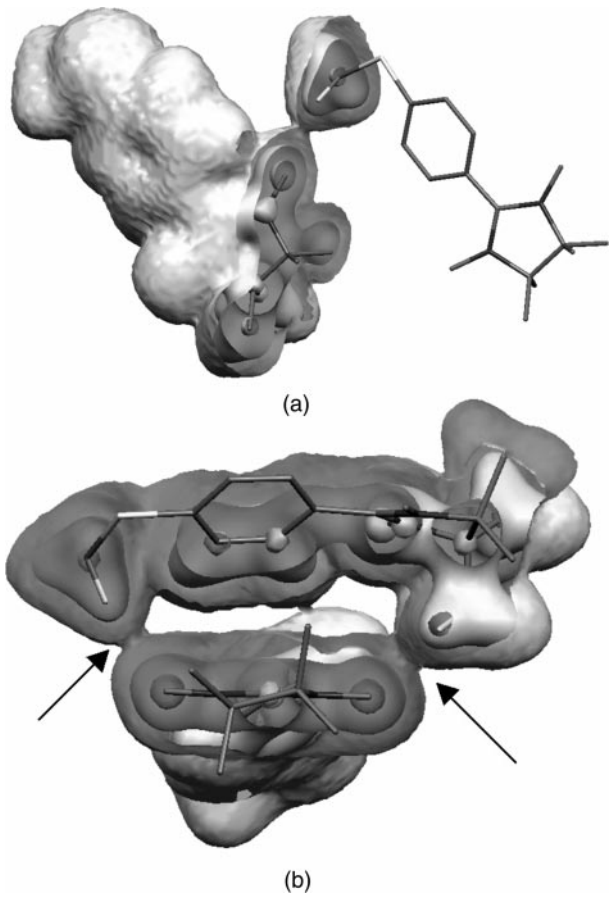

Fig. 10 Total electron density (in e Å^{-3}) in (a) the O2···H17^{ii} intermolecular contact and (b) for two molecules along the *a* axis. The molecules are oriented as in Fig. 6(a,b). In (a) isocontours are plotted at 0.03, 0.3, 3.0 e Å^{-3}. The electron density is sectioned in the O2···H17^{ii}–C14^{ii} plane. In (b) isocontours are plotted at 0.05, 0.5, 5.0 e Å^{-3}. The electron density is sectioned in the O2···N2^{i}···H8^{i} plane. The two arrows indicate the two intermolecular hydrogen bonds O1···H18^{i} and O2···H7^{i} in which electron density accumulation is present.

Discussion

The detailed structure determination, complementing the previous polarised neutron data, allows a deeper insight into the possible mechanisms leading to ferromagnetic order in Nit(SMe)Ph.[41,42]

The first clear result is that the CP topological features in the S–C5, C1–C2, C1–N1,2 bonds and in the phenyl C–C bonds are very consistent with the delocalisation scheme. They all exhibit a high mixed π-σ character (Table 8), the system being conjugated from the sulfur atom to the two oxygens.

At the end of refinement, the valence populations P_{val} show that the two N–O fragments carry a very small negative charge [−0.16(1) e]. In contrast, the methylthio fragment is highly negative, supporting the hypothesis of a charge transfer from the N2–O2–C1–N1–O1 group to C14–S. This is in agreement with the suggestion based on polarised neutron data that this is indeed an important ferromagnetic pathway. Furthermore, the presence of bond CPs between O2 and H17^{ii} in the intermolecular contact N2–O2···H17^{ii}–C14^{ii} and between O1 and H18^{i} in N1–O1···H18^{i}–C14^{i} confirms the possible interaction pathway through these two hydrogen bonds, in agreement with the significant spin population observed on C14 by polarised neutron experiments.[41,42] Even if the low electron density at these two hydrogen bond CPs is characteristic of weak interactions, the latter can be sufficient at very low temperature (close to T_c) to contribute to the ferromagnetic ordering as already observed in other nitronyl nitroxide compounds.[16,70] Therefore, as the two N–O fragments are both involved in the charge transfer with the methylthio group, this may explain the similarities observed in charges and spin populations between the two nitroxide groups. The negative charge on the sulfur atom may be due either to the intramolecular delocalisation (see above) or through these intermolecular interactions.

The O2 lone pairs are rotated in the direction of the N2–O2···O2^{i}–N2^{i} contact [Fig. 9(a)]. The length of this intermolecular contact [4.3827(5) Å] at first glance is rather long to induce molecule such effects, but is nevertheless one of the shortest observed in more than 140 studied nitronyl nitroxide compounds exhibiting magnetic behaviour.[37] However, this contact is generally believed to yield an antiferromagnetic pathway. The last contact that we wish to discuss as inducing the propagation of magnetic interactions along the *a* axis (O2···H7^{i}) is characterised by the presence of a bond CP with high electron density and Laplacian (0.06 e Å^{-3} and 1.12 e Å^{-5}, respectively). This kind of contact between the nitroxide fragment and a methyl group of the nitronyl ring has already been noted to induce ferromagnetic ordering.[33,34] Furthermore, the observed decrease of the distances in the *a* direction with temperature reinforces the interactions by these pathways. In contrast, the increase of the length in the *c* direction means that the O2···H17^{ii} hydrogen bond becomes weaker. Even if the magnetic data[39,40] show three-dimensional interactions, these features would enhance a much pronounced one-dimensional behaviour.

Conclusions

If this X-ray analysis does not replace a polarised neutron diffraction, it nevertheless gives evidence that great complementarity can be achieved on the information obtained on the magnetic interactions through these two techniques. The topological properties of the electron density allows to clearly point out the overall delocalisation scheme as well as the intermolecular interaction pathways. The atomic valence populations are consistent with a charge transfer from the O–N–C–N–O fragment to the methylthio group through two weak hydrogen bonds which are evidenced by topological analysis and consistent with the results of polarised neutron diffraction. The topological properties at the critical points in the intermolecular hydrogen bonds give more insights about the strength of the interactions compared to the geometric characteristics alone. The bulk ferromagnetic behaviour of Nit(SMe)Ph results from the presence of all these intermolecular contacts. In the *c* direction, the molecules are linked by hydrogen bonds O2···H17^{ii}–C14^{ii}. Two other hydrogen bonds (O1···H18^{i}–C14^{i} and O2···H7^{i}–C10^{i}) and intermolecular contacts O2···N2^{i} and O1···C4^{i} are responsible for the interactions in the *a* direction. The values of the electron density at the CPs in these intermolecular contacts suggest that the interactions in the *c* direction could be weaker than in the *a* direction. Finally, the competition between high thermal motion of the oxygen atoms and the deformation and rotation of their lone pairs in the direction of the intermolecular contacts could suggest that this system presents some geometric frustration effect.

Acknowledgements

This research was supported by the Centre National de la Recherche Scientifique and the Université Henri Poincaré-Nancy I. SP is grateful to the Ministère de l'Education National, de la Recherche et de la Technologie for a doctoral fellowship. DG, AC, and YP were supported by the contract ERB 40-61 PL 97-0197.

References and notes

1 E. Espinosa, E. Molins and C. Lecomte, *Phys. Rev. B*, 1997, **56**, 1820.
2 P. Delarue, C. Lecomte, M. Jannin, G. Marnier and B. Menaert, *J. Phys: Condens. Matter*., 1999, **11**, 4123.
3 P. Delarue, Ph.D. thesis, Universite Henry Poincaré-Nancy I, 1999.
4 P. Delarue, C. Lecomte, M. Jannin, G. Marnier and B. Menaert, *Eur. Phys. J. B*, 2000, **14**, 227.
5 E. Espinosa, E. Molins and C. Lecomte, *Chem. Phys. Lett*., 1998, **285**, 170.
6 E. Espinosa, C. Lecomte and E. Molins, *Chem. Phys. Lett*., 1998, **300**, 745.
7 E. Espinosa, M. Souhassou, H. Lachekar and C. Lecomte, *Acta Crystallogr., Sect. B*, 1999, **55**, 563.
8 C. Lecomte, R. H. Blessing, P. Coppens and A. Tabard, *J. Am. Chem. Soc*., 1986, **108**, 6942.
9 C. Lecomte, M. M. Rohmer and M. Benard, in *The Porphyrin Handbook*, eds. K. M. Kadish, K. M. Smith and R. Guilard, Academic Press, New York, 2000, vol. 7, p. 39.
10 V. A. Streltsov and N. Ishizawa, *Acta Crystallogr., Sect. B*, 1999, **55**, 1.
11 E. N. Maslen, V. A. Streltsov and N. Ishizawa, *Acta Crystallogr., Sect. B*, 1996, **52**, 406.
12 V. A. Streltsov and N. Ishizawa, *Acta Crystallogr., Sect. B*, 1999, **55**, 321.
13 J. F. W. Keana, *Chem. Rev*., 1978, **78**, 37.
14 O. Kahn, *Molecular Magnetism*, VCH, New York, 1993.
15 T. Sugawara, M. M. Matsushita, A. Izuoka, N. Wada, N. Takeda and M. Ishikawa, *J. Chem. Soc. Chem. Commun*., 1994, 1723.
16 J. Cirujeda, M. Mas, E. Molins, F. Lanfranc de Panthou, J. Laugier, J. G. Park, C. Paulsen, P. Rey, C. Rovira and J. Veciana, *J. Chem. Soc., Chem. Commun*., 1995, 709.
17 A. Caneschi, L. David, F. Ferraro, D. Gatteschi and A. C. Fabretti, *Inorg. Chim. Acta*, 1992, **217**, 7.
18 A. Caneschi, P. Chiesi, L. David, F. Ferraro, D. Gatteschi and R. Sessoli, *Inorg. Chem*., 1993, **32**, 1445.
19 M. G. F. Vaz, L. M. M. Pinheiro, H. O. Stumpf, A. F. C. Alcantara, S. Golhen, L. Ouahab, O. Cador, C. Mathonière and O. Kahn, *Chem. Eur. J*., 1999, **5**, 1486.
20 M. Fettouhi, M. Khaled, A. Waheed, S. Golhen, L. Ouahab, J. P. Sutter and O. Kahn, *Inorg. Chem*., 1999, **38**, 3967.
21 J. H. Osiecky and E. F. Ullman, *J. Am. Chem. Soc*., 1968, **90**, 1078.
22 K. Awaga, T. Inabe, T. Okayama and Y. Maruyama, *Mol. Cryst. Liq. Cryst*., 1993, **232**, 79.
23 K. Awaga, T. Inabe and Y. Maruyama, *Chem. Phys. Lett*., 1992, **190**, 349.
24 K. Awaga, T. Inabe, Y. Maruyama, T. Nakamura and M. Matsumoto, *Chem. Phys. Lett*., 1992, **195**, 21.
25 T. Sugano, M. Tamura, M. Kinoshita, Y. Sakai and Y. Ohashi, *Chem. Phys. Lett*., 1992, **200**, 235.
26 P. Turek, K. Nozawa, D. Shiomi, K. Awaga, T. Inabe, Y. Maruyama and M. Kinoshita, *Chem. Phys. Lett*., 1991, **180**, 327.
27 Y. Hosokoshi, M. Tamura and M. Kinoshita, *Mol. Cryst. Liq. Cryst*., 1993, **232**, 45.
28 K. Awaga and Y. Maruyama, *Chem. Phys. Lett*., 1989, **158**, 556.
29 K. Awaga, T. Inabe, U. Nagashima and Y. Maruyama, *J. Chem. Soc., Chem. Commun*., 1989, 1617.
30 H. M. McConnell, *J. Phys. Chem*., 1963, **39**, 1910.
31 H. M. McConnell, *Proc. R. A. Welch Found. Conf. Chem. Res*., 1967, **11**, 144.
32 J. Veciana, J. Cirujeda, C. Rovira and J. Vidal–Gancedo, *Adv. Mater*., 1995, **7**, 221.
33 J. Cirujeda, E. Hernandez–Gasio, C. Rovira, J. L. Stanger, P. Turek and J. Veciana, *J. Mater. Chem*., 1995, **5**, 243.
34 M. M. Matsushita, A. Izuoka, T. Sugawara, T. Kobayashi, N. Wada, N. Takeda and M. Ishikawa, *J. Am. Chem. Soc*., 1997, **119**, 4369.
35 K. Awaga, T. Sugano and M. Kinoshita, *Chem. Phys. Lett*., 1987, **141**, 540.
36 J. J. Novoa, M. Deumal and J. Veciana, *Synth. Met*., 1999, **103**, 2283.
37 M. Deumal, J. Cirujeda, J. Veciana and J. J. Novoa, *Chem. Eur. J*., 1999, **5**, 1631.
38 C. K. Johnson, ORTEP II, Report ORNL-5738, Oak Ridge National Laboratory, Oak Ridge TN, USA, 1976.
39 A. Caneschi, F. Ferraro, D. Gatteschi, A. Le Lirzin and E. Rentschler, *Inorg. Chem. Acta*, 1995, **235**, 159.
40 A. Caneschi, F. Ferraro, D. Gatteschi, A. Le Lirzin, M. Novak, E. Rentschler and R. Sessoli, *Adv. Mater*., 1995, **7**, 476.
41 Y. Pontillon, A. Caneschi, D. Gatteschi, E. Ressouche, J. Schweizer and R. Sessoli, *Physica B (Amsterdam)*, 1999, 51.
42 Y. Pontillon, A. Caneschi, D. Gatteschi, A. Grand, E. Ressouche, R., Sessoli and J. Schweizer, *Chem. Eur. J*., 1999, **5**, 3616.
43 Z. Otwinowski and W. Minor, in *Methods in Enzymology*, eds. C. W. Carter, Jr. and R. M. Sweet, Academic Press, New York, 1996, p. 276.
44 R. H. Blessing, *J. Appl. Crystallogr*., 1989, **22**, 396.

45 S. Kuntzinger, S. Dahaoui, N. E. Ghermani, C. Lecomte and J. A. K. Howard, *Acta Crystallogr., Sect.*, B, 1999, **55**, 867.
46 C. Wilkinson, H. W. Khamis, R. F. D. Stansfield and G. J. McIntyre, *J. Appl. Crystallogr.*, 1988, **21**, 471.
47 P. J. Brown and J. C. Mattheman, *The Cambridge Crystallographic Subroutine Library*, RL-81-063, ILL, Grenoble.
48 N. K. Hansen and P. Coppens, *Acta Crystallogr., Sect. A*, 1978, **34**, 909.
49 E. J. Gabe, Y. Le Page, J. P. Charland and F. L. Lee, *J. Appl. Crystallogr.*, 1989, **22**, 384.
50 S. Dahaoui, V. Pichon–Pesme, J. A. K. Howard and C. Lecomte, *Acta Crystallogr., Sect. B*, 1999, **55**, 226.
51 E. Clementi and C. Roetti, *At. Data Nucl. Data Tables*, 1974, **14**, 177.
52 *International Tables of Crystallography*, Reidel, Dordrecht, 1992, vol. C, p. 219.
53 P. Coppens, *X-Ray Charge Densities and Chemical Bonding*, IUCr, Oxford University Press, Oxford, 1997.
54 C. Lecomte, in *The Application of Charge Density Research to Chemistry and Drug Design*, ed. G. A. Jeffrey and J. F. Piniella, NATO ASI Series, Plenum, New York, 1991, vol. B250, p. 155.
55 R. F. W. Bader, *Atoms in Molecules: a Quantum Theory*, The International Series Monographs in Chemistry, Clarendon Press, Oxford, 1990.
56 M. Souhassou and R. H. Blessing, *J. Appl. Crystallogr.*, 1999, **32**, 210.
57 U. H. Zucker and H. Schulz, *Acta Crystallogr., Sect. A*, 1982, **38**, 563.
58 P. Coppens, T. N. Guru Row, P. Leung, E. D. Stevens, P. J. Becker and Y. W. Yang, *Acta Crystallogr., Sect. A*, 1979, **35**, 63.
59 U. H. Zucker, E. Perenthaler, W. F. Kuhs, R. Bachmann and H. Schulz, *J. Appl. Crystallogr.*, 1983, **16**, 358.
60 B. T. M. Willis and A. W. Pryor, *Thermal Vibrations in Crystallography*, Cambridge University Press, Cambridge, 1975.
61 V. Schomaker and K. N. Trueblood, *Acta Crystallogr., Sect. B*, 1968, **24**, 63.
62 X. M. He and B. M. Craven, *Acta Crystallogr., Sect. A*, 1993, **49**, 10.
63 F. L. Hirshfeld, *Acta Crystallogr., Sect. A*, 1976, **32**, 239.
64 The failure of the rigid bond test may also be due to the experimental limit of resolution, which could prevent the model from fully deconvoluting thermal motion and electron density parameters.
65 To simplify the notations, the following definition for symmetry-related atoms are used: *i* for the glide plane $(1/2 + x, 1/2 - y, z)$ and *ii* for the cell translation $(x, y, 1 - z)$.
66 M. Souhassou, C. Lecomte, R. H. Blessing, A. Aubry, M. M. Rohmer, R. Wiest, M. Benard and M. Marraud, *Acta Crystallogr., Sect. B*, 1991, **47**, 253.
67 B. Fabius, C. Cohen–Addad, F. K. Larsen, M. S. Lehmann and P. Becker, *J. Am. Chem. Soc.*, 1989, **111**, 5728.
68 S. K. Yeh and Y. Wang, *Acta Crystallogr., Sect. B*, 1992, **48**, 319.
69 M. Souhassou, C. Lecomte, N. E. Ghermani, M. M. Rohmer, R. Wiest, M. Benard and R. H. Blessing, *J. Am. Chem. Soc.*, 1992, **114**, 2371.
70 T. Sugawara, M. M. Matsushita, A. Izuoka, N. Wada, N. Takeda and M. Ishikawa, *J. Chem. Soc., Chem. Commun.*, 1994, 1723.